OBSERVATIONAL UPPER LIMITS FOR LOW-DEGREE SOLAR G MODES

T. Appourchaux[1], C. Fröhlich[2], B. Andersen[3], G.Berthomieu[4], W. J. Chaplin[2,5],
Y. Elsworth[5], W. Finsterle[1], D. O. Gough[6,7], J .T. Hoeksema[8], G. R. Isaak[5],
A. G. Kosovichev[8], J. Provost[4], P. H. Scherrer[8], T. Sekii[6], T. Toutain[4]

ABSTRACT

Observations made by the Michelson Doppler Imager (MDI) and Variability of solar IRradiance and Gravity Oscillations (VIRGO) on the Solar and Heliospheric Observatory (SOHO) and by the ground-based Birmingham Solar Oscillations Network (BiSON) and Global Oscillations Network Group (GONG) have been used in a concerted effort to search for solar gravity oscillations. All spectra are dominated by solar noise in the frequency region from 100 to 1000 μHz where g modes are expected to be found. Several methods have been used in an effort to extract any g-mode signal present. These include: (i) the correlation of data – both full-disc and imaged (with different spatial-mask properties) – collected over different time intervals from the same instrument, (ii) the correlation of near-contemporaneous data from different instruments, and (iii) the extraction – through the application of complex filtering techniques – of the coherent part of data collected at different heights in the solar atmosphere.

The detection limit is set by the loss of coherence caused by the temporal evolution and the motion (e.g. rotation) of superficial structures. Although we cannot identify any g-mode signature, we have nevertheless set a firm upper limit to the amplitudes of the modes: at 200 μHz, they are below $10\,\mathrm{mm\,s^{-1}}$ in velocity, and below 0.5 parts per million in intensity. The velocity limit corresponds very approximately to a peak-to-peak vertical displacement of $\delta R/R_\odot = 2.3 \cdot 10^{-8}$ at the solar surface. These levels which are much lower than prior claims, are consistent with theoretical predictions.

Subject headings: Sun: general – Sun: interior – Sun: oscillations – methods: data analysis

1. INTRODUCTION

Helioseismology has, over the past twenty five years, added immensely to our knowledge of the solar interior through the study of resonant p-mode oscillations. (See Christensen-Dalsgaard 1998 for a recent review of the field.) The current seismic signal are the manifestation of sound waves trapped within the body of the Sun. Gravity g modes remain undetected.

Sound waves which traverse the solar interior spend little time in the core regions, owing to the very high temperature. In spite of this short dwell time, the p modes are nonetheless a sensitive probe of the deep radiative interior since their frequencies can be measured to such high accuracy (a few parts in 10^6 for the lowest-frequency low-degree p modes detected to date). However, the g modes we seek to detect would be confined wholly within a resonant cavity in the radiative interior. Their detection there-fore promises to provide an even more precise diagnostic of the core properties of the Sun. Since they are evanescent in the convection zone, the amplitudes of these modes are expected to be very low in the photosphere where the responses of the most commonly used observational techniques are peaked. This makes the task of obtaining a firm detection particularly challenging. In addition, the predicted g-mode amplitudes before the launch of SOHO were about 1 mm s^{-1} (Gough 1985). In view of the predicted solar noise (Harvey 1985), this made the detection of g modes a challenging task.

The first claims of detection of solar normal modes at frequencies below $500\,\mu$Hz were made by a number of groups using different techniques. Severny et al. (1976) measured the difference between the radial velocity of a central portion and a circular annulus of the solar disc, and found a signal with period 160 minutes and ampli-

[1] Space Science Department, P.O.Box 299, NL-2200AG Noordwijk, The Netherlands

[2] Physikalisch-Meteorologisches Observatorium Davos, World Radiation Center, CH-7260 Davos Dorf, Switzerland

[3] Norwegian Space Centre, N-0212 Oslo, Norway

[4] Département Cassini, UMR CNRS 6529, Observatoire de la Côte d'Azur, F-06304 Nice, France

[5] School of Physics and Astronomy, University of Birmingham, Edgbaston, Birmingham, B15 2TT, United Kingdom

[6] Institute of Astronomy, University of Cambridge, Cambridge CB3 OHA, United Kingdom

[7] Department of Applied Physics and Theoretical Physics, University of Cambridge, Cambridge CB3 9EW, United Kingdom

[8] W.W.Hansen Experimental Physics Laboratory, Stanford University, Stanford, CA 94305, USA

tude $2.2\,\mathrm{m\,s^{-1}}$. Brookes et al. (1976) searched for minute radial velocity variations analogous to those of Cepheids and other pulsating stars. From the analysis of two days of data, they uncovered the presence of a statistically highly significant periodic signal at 2.65 hours with an associated amplitude of $2.7\,\mathrm{m\,s^{-1}}$. Later comparison between the two sets of measurements established that the oscillation phases of the two agreed. Brown et al. (1978) measured the diameter of the Sun using sophisticated edge-definition observations. To date, it is not clear whether the claimed oscillations were due to atmospheric disturbances or instrumental artifacts, or to temporal variations of true solar origin which have since subsided.

These early observations were followed up by numerous other measurements giving ever decreasing amplitudes or amplitude limits (e.g. Scherrer et al. 1979, Delache & Scherrer 1983). Subsequent intensity and Doppler velocity observations have failed to confirm these results. (For a review see Fröhlich & Andersen 1995.) More recently, Thomson et al. (1995) claim to have detected g modes in solar wind data collected by *Ulysses* (Marsden et al. 1996). However, this has now been cast into some doubt as the result of further analyses (Riley & Sonett 1996, Hoogeveen & Riley 1998, Denison & Walden 1999).

The modern field of helioseismology supports a broad range of high-quality observational programs, both space-borne (e.g. GOLF[1], VIRGO[2] and MDI[3] on board the SOHO[4] spacecraft) and ground-based (e.g. BiSON[5], GONG[6], IRIS[7] and LOWL/ECHO[8]). Here, we report on attempts to detect low-degree g modes through the coordinated use of near-contemporaneous data collected by the VIRGO, MDI, BiSON and GONG programs. We describe in detail the various analysis strategies we have adopted. Particular attention is paid to the non-trivial issue of the precise calibration and comparison of frequency spectra generated from data collected in intensity and velocity. While we have failed to detect g modes, we have nevertheless placed the lowest limits to date on their amplitudes. The failure to detect any g mode is a confirmation of theoretical predictions (Gough 1985, Harvey 1985)

2. OBSERVATIONS

2.1. *MDI data*

The MDI data (Scherrer et al. 1995) used here are the LOI-proxy velocities (Hoeksema et al. 1998). They consist of a set of calibrated velocities measured in the 180

bins of the LOI-proxy "instrument" over a period of 784 days (from 1996 May 1 to 1998 June 23). The trend due to the radial orbital velocity of the spacecraft has been removed from the data using information contained in the SOHO orbit data files, and the remaining exponential trend removed by subtracting a boxcar average of width 1 day applied to the time series. The data have a sampling cadence of 15 sec (Nyquist frequency at 33.3 mHz) and an integration time of 1 %. The complete time series has a duty cycle of better than 98%. Individual time series were built for each (l, m) mode with spherical-harmonic masks.

2.2. *VIRGO data*

A detailed description of the instruments which comprise VIRGO, their operation and data acquisition procedures is given by Fröhlich et al. (1995). The data from PMO6V, SPM and LOI used in the present analysis are described in the following sections.

2.2.1. *Total and spectral irradiance*

The PMO6V and DIARAD radiometers measure the total solar irradiance (TSI), while the sunphotometers (SPM) measure the spectral irradiance in three 5-nm-wide spectral bands in the red (862nm), green (500nm) and blue (402nm) parts of the spectrum. The sampling cadence of the SPM is 60 s (Nyquist frequency at 8.3 mHz) with an integration time of 94%. The sampling cadence of the radiometers is 180 s (Nyquist frequency at 2.78 mHz) and an integration time of 31.3%. The performance of these instruments is described by Anklin et al. (1998). For the present study, we use data from the PMO6V radiometer and the SPM.

The total length of the time series used is 853 days, starting 1996 February 22. The duty cycles are 94.1% for the PMO6V, and 92.7%, 95.2%, and 95.8% for the red, green, and blue SPM channels respectively. Because the sensitivity of the SPM – and to a much lesser extent that of the radiometer – have suffered degradation over the course of the mission, proper de-trending of the time series is essential. A triangular-shaped filter of FWHM 1 day has been used to de-trend the time series and to calculate the relative variations.

2.2.2. *Luminosity Oscillation Imager*

The performance of the Luminosity Oscillation Imager (LOI), and the associated data-reduction procedures, are

---

[1]Global Oscillations at Low Frequency

[2]Variability of solar IRradiance and Gravity Oscillations

[3]Michelson Doppler Imager

[4]Solar and Heliospheric Observatory, an ESA/NASA Mission

[5]Birmingham Solar-Oscillations Network

[6]Global Oscillation Network Group

[7]Investigation on the Rotation and Interior of the Sun

[8]The low-l instrument

described by Appourchaux et al. (1997). Each pixel is detrended with a triangular-shaped filter of FWHM 1 day. In order to extract a given angular degree, the 12 pixels are combined using spherical harmonic filters (Appourchaux & Andersen 1990, Appourchaux et al. 1998b). Since these filters are complex, they allow one to separate each m in a given (l, n) multiplet. The leakage properties of the filters are well known (Appourchaux et al. 1998b). The filters are computed on a weekly basis using the real size of the solar image – which is calibrated in flight – and the orientation (latitude) angle of the Sun. (The position angle of the solar rotation axis is maintained at zero degrees by the orientation of the spacecraft.) The weekly filters are then averaged over the duration of the observations in order to produce a single filter which can be applied to the pixel time series to produce the targeted (l, m) signal. The sampling cadence of the LOI is 60 s (Nyquist frequency at 8.3 mHz) and an integration time of 99%. The time series utilized here is of length 819 days (from 1997 March 27, 1996 through 1998 June 24), and has a 99% duty cycle.

2.3. *BiSON data*

BiSON is a network of 6 stations distributed around the globe (Elsworth et al. 1995). The instruments use a Potassium resonance cell to measure solar radial velocities (Brookes et al. (1978b)). The sampling cadence of BiSON is typically 40 s (Nyquist frequency at 12.5 mHz) with a typical integration time of 40%.

Unlike those derived from the SOHO instruments, a BiSON frequency spectrum is generated from an appropriate (coherent) combination of data collected by six network instruments. The comparative quality of the data will inevitably vary, with some stations better suited to the study of low-frequency phenomena than others. In order to maximize one's ability to detect long-period solar p and g modes, data selection criteria are required that take into account the quality of the observations made at each site over the frequency range of interest. The need to maximize the duty cycle of the network implies that data should be used, where available, from a single station. However, there is a trade-off between: (i) the introduction of these data to the final time series; and (ii) the possibility that—if they are of poor quality—their use may drive up the noise power level of the combined network set to such an extent that this negates the apparent advantage of using the data in the first place.

The above can be expressed quantitatively as follows. First, consider a time series comprised of data from a single site. Let d be the fractional duty cycle of the time series, and $P(\nu)$ be the mean spectral noise power over the targeted frequency range (say, $\nu \rightarrow \nu + \delta\nu$). A simple "Figure Of Merit" (F.O.M) that encapsulates the trade-off is then:

$$\text{F.O.M} = d/P(\nu). \qquad (1)$$

For $d = 1.0$, i.e., a 100% fill in the time domain, the F.O.M.

in Eq. (1) then corresponds simply to the inverse of the mean power over the frequency band of interest. If data are to be combined from several stations, this expression must be generalized somewhat. If the characteristics of the constituent sites are each tagged by the index i, such that for N stations, $1 \leq i \leq N$, the expanded expression becomes:

$$\text{F.O.M} = \frac{D^2}{\sum\limits_{i=1}^{N} d_i \cdot P_i(\nu)}, \qquad (2)$$

where

$$D = \sum_{i=1}^{N} d_i. \qquad (3)$$

As a first cut at the problem, we have implemented a set of code that makes use of the above in the following manner. Let $p_i(\nu, t)$ be the mean power, calculated over the target frequency range, on a day-by-day basis. Next consider a daily power rejection threshold for each site $T_i(\nu, t)$, again appropriate to the targeted frequency range. If we choose to reject individual days for which the the power $p_i(\nu, t) > T_i(\nu, t)$, this will alter: (i) $P_i(\nu)$, i.e., the overall mean power contribution from site i; and (ii) f_i, the fractional fill contribution from the site. Clearly, we wish to find some combination of site thresholds, $T_i(\nu, t)$ that will give the optimal overall combination, i.e., that which maximizes the F.O.M.. This can be realized by, in essence, performing a multi-parameter minimization – here, one varies, and then seeks to find at convergence, optimal estimates of the power rejection thresholds for each site. Here we should point out that our optimization procedure does not filter out any low frequency component.

The resulting procedure has been applied in order to select data – collected over the period 1994 May 16 through 1997 Jan 10 (971 days) – in order to optimize the combined BiSON time series for the frequency range $200 \leq \nu \leq 1000 \, \mu\text{Hz}$. The post-optimization duty cycle is about 61% (reduced from 75%). At frequencies below $\sim 200 \, \mu\text{Hz}$, contamination by window-function-related artifacts becomes severe; however, this is not of serious concern since the strongest g modes (i.e., those most-likely to be detected first) are expected to be found at higher frequencies.

2.4. *GONG data*

GONG consists of 6 stations distributed around the globe (Harvey et al. 1996). Each instrument measures solar radial velocities in the NiI 676.8-nm line with a Michelson interferometer. The GONG data reduction procedures are described by Hill et al. (1996). In order to extract the mode signal, spherical-harmonic filters are applied to the pixel time series in a manner similar to the MDI and LOI data. In addition, the mean velocity is subtracted from each image. Unfortunately, this subtraction –

combined with a merging optimized for the p-mode range – enhances considerably the low frequency noise. Consequently we choose to use only the available full-disc integrated signal (which remains unaffected). The sampling cadence of GONG is 60 s (Nyquist frequency at 8.3 mHz) and an integration time of 33%. The time series used is of length 1260 days (spanning the period 1995 May 24 through to 1998 September 29), and has a duty cycle of 84%.

The standard GONG pipeline reduction procedures are tailored to the higher-frequency p-mode range, and as such, a difference filter is applied to the time series in order to suppress very low-frequency drifts in the data. Since these frequencies are of interest to us here, we have recovered this information by dividing the computed GONG power spectrum by the corresponding transfer function, e.g. $f(\nu) = 4\sin^2(\pi\nu\Delta t)$, where ν is the frequency and Δt=60 sec is the sampling time (Hill and Leibacher, 1999, private communication).

3. ANALYSIS TECHNIQUE

In order to compare the data from the different instruments, we need to take into account the fact that: (i) the temporal and spatial filtering appropriate to the different observations will differ; and (ii) the observational responses may be peaked at different heights in the solar atmosphere. Here, we address these issues in turn, before considering in detail the techniques of analysis that we have applied in an effort to uncover g modes in our data.

3.1. *Spatial and temporal filtering*

3.1.1. *Temporal filtering*

All power spectra computed for this paper have been divided by the associated fractional duty cycle, $\mathcal{F}$, such that for a time-series of length N samples a white-noise (Gaussian) source with a zero mean, characterized by a sample standard deviation of σ, will give a mean power level in the frequency domain of σ^2/N. This means that they satisfy Parseval's theorem.

In order to ascribe the height of a prominent, narrow peak in such a spectrum to an associated signal amplitude in the time domain, we must allow properly for the fill. Consider first a coherent, periodic signal (e.g., a sine wave) with associated amplitude A. A power spectrum of a gap-free signal will have a peak of height A^2. If the same signal is now forced through a window function with fractional duty cycle $\mathcal{F}$, the presence of gaps in the time domain will result in a redistribution of power from the main signal peak into, for example, prominent sidebands if the gap structure has a strong periodic component. The height of the main peak will be reduced to $\mathcal{F}A^2$. All spectra shown are scaled to amplitude on the ordinate. In order to recover correctly an estimate of the amplitude of a signal which gives a prominent peak in the power spectrum, its measured height must be divided by the square root of

the fractional fill. This compensates for the power aliased out of the peak.

Apart from the obvious correction performed on the GONG data, no attempt was made to correct the spectra from the different detrending filters or integration windows. Nevertheless we can assess their influence on the spectra. The 1-day boxcar filter will produce a 11.57-μHz sinusoidal modulation of power present in the frequency domain, with an amplitude of $\approx$ 1% above 300 μHz; around 100 μHz the modulation increases to $\pm$ 4 %. The 1-day triangle filter will modulate power by less than 0.2% at 100 μHz. As mentioned in a previous section the GONG detrending filter produces much larger disturbances that needed correction; this is not required for the other filters. The additional filtering effect of the integration window is rather negligible for the low-frequency part of the spectrum; it does, however, have some effect over the p-mode range when the integration time is close to 100%. This window also introduces spurious power from the aliasing of high frequency power. The power aliasing at low frequencies depends on the quality of the integration time and on the solar spectrum. When the integration time is high ($\approx$ 100 %), the aliased solar spectrum at low frequencies is filtered out by the integration window; this is the case for VIRGO/SPM and VIRGO/LOI. For the other instruments, which have a lower integration time, the aliased power is fully transmitted. However owing to the $1/f$ characteristics of the solar spectrum, 1% at most of the power is aliased into the low-frequency band (the worst case figure is given for the VIRGO radiometers). The low-frequency spectra presented in this paper are therefore negligibly affected by the aliased power and the detrending filters.

3.1.2. *Spatial filtering*

We must also take into account the spatial filter functions S_{nlm} of each instrument. These are defined such that the observed RMS velocity, v_{obs}^{nlm}, of a mode identified by (n, l, m) is calibrated so as to yield its RMS value over time and space as:

$$v_{\text{obs}}^{nlm} = S_{nlm} v_{\text{rms}}^{nlm} \qquad (4)$$

The appendix gives a proper definition of the spatial filter function, which should not be confused with the visibility. Dziembowski (1977), Brookes et al. (1978a) and Christensen-Dalsgaard (1989) have, amongst others, discussed issues relating to the spatial filter functions appropriate to full-disc observations. Here, we have derived the spatial filter functions for both the full-disc and imaging observations (See Tables 1 and 2). Their derivations are given in the appendix. These have been checked for consistency by applying the corrections to the various calibrated spectra and comparing the resulting mode amplitudes at the center of the p-mode spectrum (i.e.,

TABLE 1

P-MODE SPATIAL FILTER FUNCTIONS OF THE FULL-DISC
INTEGRATING INSTRUMENTS.

l	m	S_{lm}^{Blue}	S_{lm}^{Green}	S_{lm}^{Red}	$S_{lm}^{\mathrm{BiSON}\dagger}$
0	0	1.00	1.00	1.00	0.72
1	0	0.00	0.00	0.00	0.00
1	1	0.90	0.88	0.85	0.70
2	0	0.41	0.38	0.34	0.33
2	1	0.00	0.00	0.00	0.00
2	2	0.50	0.46	0.41	0.50

$\dagger$ The BiSON values have been corrected for Doppler imaging effects as computed by Christensen-Dalsgaard (1989).

TABLE 2

P-MODE SPATIAL FILTER FUNCTIONS OF THE IMAGING INSTRUMENTS

l	m	S_{lm}^{LOI}	S_{lm}^{MDI}	S_{lm}^{GONG}
0	0	1.16	1.00	0.70
1	0	0.87	1.00	$\cdots$
1	1	1.24	1.00	$\cdots$
2	0	0.86	1.00	$\cdots$
2	1	1.01	1.00	$\cdots$
2	2	1.21	1.00	$\cdots$

at a frequency of $\sim 3\,\mathrm{mHz}$). When we do so, we find that the velocity spectra all give maximum amplitudes of $\sim 20\,\mathrm{cm\,s^{-1}}$.

The comparison of amplitudes observed in the full-disc LOI data and the green channel of the SPM (nearest wavelength, and hence closest response height, to the LOI value) also validates the spatial filter functions computed in intensity.

It is, in principle, possible to compute the corresponding spatial filter functions for the g modes. They are highly frequency and degree dependent. However, since any computation of the intensity filter functions rely heavily on uncertain theoretical considerations, we choose here not to compute the spatial filter functions for the g modes. Instead we use the spatial filter functions for the p-mode frequencies and apply them in the g-mode frequency regime.

3.2. Observation heights in the atmosphere for acoustic waves

The trapped p modes and core-penetrating g modes are evanescent in the photosphere, where the instruments detect either intensity changes or spectral line shift interpreted as Doppler velocity variations. While the energy density of the modes therefore decreases with height, the decreasing mass density of the atmosphere means that the amplitude of the observed waves actually increases with increasing altitude.

The LOI and SPM both possess an observational response that is peaked very close to $0\,\mathrm{km}$, i.e., at the base of the photosphere[9], while the BiSON, GONG and MDI velocity data reflect perturbations roughly $250-300\,\mathrm{km}$ above this level. We stress here that these values are very approximate, and a precise derivation is far from trivial. In addition, due to dependence on averaging of surface fine structure, an average mean formation height may be physically irrelevant. As such, our intention here is merely to flag the issue of height dependence, i.e., we have not attempted to re-normalize any of the data to a notional reference height.

A proper derivation requires a thorough treatment of the radiation hydrodynamics of the Fraunhofer line used (KI for BiSON, NiI for GONG and MDI), which gives the observations a different weighting over the solar disc. In addition, for GONG and MDI the observation height differs from that of the line formation height (Jones 1989). Further, the observation height changes over the course of the observing season – again, to an extent which depends upon the observational technique – as the passbands of the instrument sweep over the wings of the line, reflecting the changing relative velocity between different part of the Sun and the instrument. Clearly, this effect will be more pronounced for the ground-based data, and raises subtle issues regarding the manner in which contemporaneous observations from different sites in a network, whose longitudes may differ by several tens of degrees, are combined to yield the final coherent time series.

3.3. Statistical analysis

The statistical distribution that describes power spectra made from either full-disc or resolved-image data can be approximated by χ^2 with n d.o.f, where $n = 2$ for full-disc integrating instruments, and $n > 2$ for resolved data. This information can be used to derive the power level at which a peak due to noise has a probability, p_{det}, of appearing over a given range in frequency, Δ_{det}. This threshold depends upon the observing time (T), since the number of frequency bins over the considered bandwidth will increase with the length of the time series. The probability that a random variable X takes a value higher than a given value x is given by:

$$p(x < X) = \frac{\Gamma(n/2, x/2)}{\Gamma(n/2)}, \qquad (5)$$

where $\Gamma(a, x') = \int_{x'}^{+\infty} e^{-t} t^{a-1} dt$, and $\Gamma(a)$ is the Gamma function. Therefore the probability, p_{det}, that at least one out of N peaks be higher than a given value, x, is given by:

$$p_{\mathrm{det}} = 1 - (1 - p(x < X))^N. \qquad (6)$$

If $p(x < X)$ is small, we then have:

$$p_{\mathrm{det}} \approx N p(x < X). \qquad (7)$$

Since $N = T \Delta_{\mathrm{det}}$, combining the above gives:

$$p_{\mathrm{det}} \approx T \Delta_{\mathrm{det}} \left(\frac{\Gamma(n/2, x/2)}{\Gamma(n/2)} \right). \qquad (8)$$

Equation (8) can be used to derive the relative level s_{det} (measured in units of the mean, $\tilde{s}$, over the chosen frequency range of the spectrum) which corresponds to a given probability p_{det} for a chosen window and observing time.

3.3.1. Analysis of full-disc integrated data

The statistical distribution of power spectra made from full-disc integrated observations is known to be χ^2 with 2 d.o.f.[10] In this case we can write:

$$\frac{\Gamma(1, x/2)}{\Gamma(1)} = e^{-\frac{x}{2}} \qquad (9)$$

by replacing $x/2$ by $s_{\mathrm{det}}/\tilde{s}$ in Eq. (9), we can solve analytically Eq. (8) to yield:

$$\frac{s_{\mathrm{det}}}{\tilde{s}} \approx \ln(T) + \ln(\Delta_{\mathrm{det}}) - \ln(p_{\mathrm{det}}), \qquad (10)$$

---

[9]Here, we define the base of the photosphere to be where optical depth reaches unity at a wavelength of $500\,\mathrm{nm}$. Note that solar models are usually normalized to unity radius where $T = T_{\mathrm{eff}}$; this height lies some $\sim 50\,\mathrm{km}$ above our chosen radial datum.

[10]This is not strictly correct if there are gaps in the time domain, which remove the statistical independence of bins in the frequency domain.

where T is in units of 10^6 sec and Δ_{det} is given in μHz. So, for a ≈ 70-μHz bandwidth, a 1-year observing time and a probability level of 10%, the absolute detection level corresponds to 10 $\tilde{s}$. (Note that the 70-μHz band is approximately the separation of adjacent low-degree p-mode pairs; the band was adjusted slightly to yield the 10-$\tilde{s}$ level.) We computed thresholds for detectable modes at the low-frequency end of the p-mode spectrum in order to establish that the 10-$\tilde{s}$ level constitutes a meaningful detection criterion.

All levels hereafter are computed according to the 10-$\tilde{s}$ baseline – taking into account the observing time – such that s_{det} can be re-expressed according to:

$$\frac{s_{\mathrm{det}}}{\tilde{s}} \approx 10 + \ln(T_y), \qquad (11)$$

where T_y is now given in years.

If we were to use only prejudice to guide our efforts to detect g modes, we might choose to home in on rather narrower bandwidths (i.e., in the vicinity of the model frequencies) of order 1 μHz or less. The corresponding 10% threshold would then be reduced to $s_{\mathrm{det}}/\tilde{s} = 5.75$. However, because of the bandwidth reduction, one is likely to find rogue candidate peaks close to the theoretical frequencies if one maintains the 10% detection criterion. For example, the probability of having at most one peak higher than $s_{\mathrm{det}}/\tilde{s} = 5.75$ out of 20 1-μHz windows is about 39 %. Therefore, the probability of having at least 2 peaks appearing in 20 similar windows is 61 %, i.e., the likelihood of finding prominent peaks which are simply part of the background noise distribution is then quite high. The utilization of a large window (e.g. 70 μHz) will be less subject to spurious detection.

Figure 1 shows the amplitude spectra of the three SPM channels and the full-disc LOI data. The upper detection limit for the red SPM is about 0.5 ppm at 200 μHz, and 0.3 ppm at 1000 μHz. The levels for the other colors scale approximately with the temperature perturbation induced on the blackbody spectrum, with a slightly lower signal-to-noise ratio in the blue channel. The noise in the LOI amplitude spectrum is about 10% higher than the green SPM above 200 μHz, and 30% higher below. The additional noise comes from several sources. The most important are probably small variations in the image size over the detector and the effect of structures rotating into and out of the non-sensitive inter-pixel areas of the detector.

Figure 2 displays the amplitude spectra for the velocity instruments that observe the Sun as a star. The MDI data contain harmonics of 52.125 μHz, which arise from beats between the spacecraft timing system and the instrument sampling rate. We have removed these from the spectrum displayed in the figure. The presence of gaps in the GONG and BiSON data gives rise to daily harmonics at very low frequencies that have not been removed.

The solid line in each panel indicates the 10% threshold level as a function of frequency. We stress again that the ordinate of each spectrum is scaled such that a commensurate sine wave with amplitude A will give a peak of amplitude $\sqrt{\mathcal{F}}A$ in the frequency domain. The upper detection limit is: for MDI, 15 mm s^{-1} at 200 μHz, and 6 mm s^{-1} at 1000 μHz; for BiSON, 12 mm s^{-1} at 200 μHz, and 4 mm s^{-1} at 1000 μHz; and for GONG, 20 mm s^{-1} at 200 μHz, and 5 mm s^{-1} at 1000 μHz. Taking into account the spatial filter functions, the MDI levels are typically 20-50% lower than those of GONG; in comparison, the BiSON instrument performs almost as well as MDI above 400 μHz.

3.3.2. *Analysis of resolved LOI, MDI and GONG data*

Various pattern-recognition techniques have been used in an effort to reveal the presence of g modes. All assume that the modes are split by rotation and (or) that their frequencies can be derived from an asymptotic formula (Fröhlich & Andersen 1995, Fröhlich & Delache 1984). For the resolved-Sun data, we have devised a new pattern technique for detecting the modes.

A *collapsogramme* is constructed from the m spectra available at a chosen (n,l). Each m spectrum is shifted from the $m = 0$ spectrum by $\delta_{nlm} = m\Omega_{nlm}$ (where Ω_{nlm} represents the splitting of the mode), and is then normalized by an estimate of the variance of the spectrum in the narrow frequency range of interest. The application of the variance renormalization procedure means that the collapsogramme differs from the well-known m-averaged spectrum, where the constituent sets are combined with equal weight. The resulting $2l+1$ shifted and renormalized spectra are then each divided by the appropriate (l,m) spatial filter functions, and co-added to yield the collapsogramme (which is itself renormalized for comparison with individual or full-disc spectra). The equation for the collapsed spectrum is therefore:

$$s_l(\nu) = \sum_{m=-l}^{m=l} w_m F_m^l(\nu - m\Omega_{nlm}), \qquad (12)$$

where $F_m^l(\nu)$ is the spectrum corrected for the spatial filter functions for a given (l,m), and the weights w_m are given by:

$$w_m = \left(\frac{1}{\sum_{m=-l}^{m=l} \frac{1}{\tilde{f}_m}} \right) \frac{1}{\tilde{f}_m}. \qquad (13)$$

In the above, $\tilde{f}_m$ is an estimate of the mean of the power spectrum in a narrow frequency band (700 to 800 μHz).

The use of this simple procedure is appealing since it effectively dilutes instrumental harmonics (which are invariant), and produces a spectrum with well defined statistics (very nearly χ^2 with $4l + 2$ d.o.f.). However, since the rotational splitting of the g modes is expected to vary rather more with frequency than for p modes, the technique must be applied either: (i) over a band in frequency
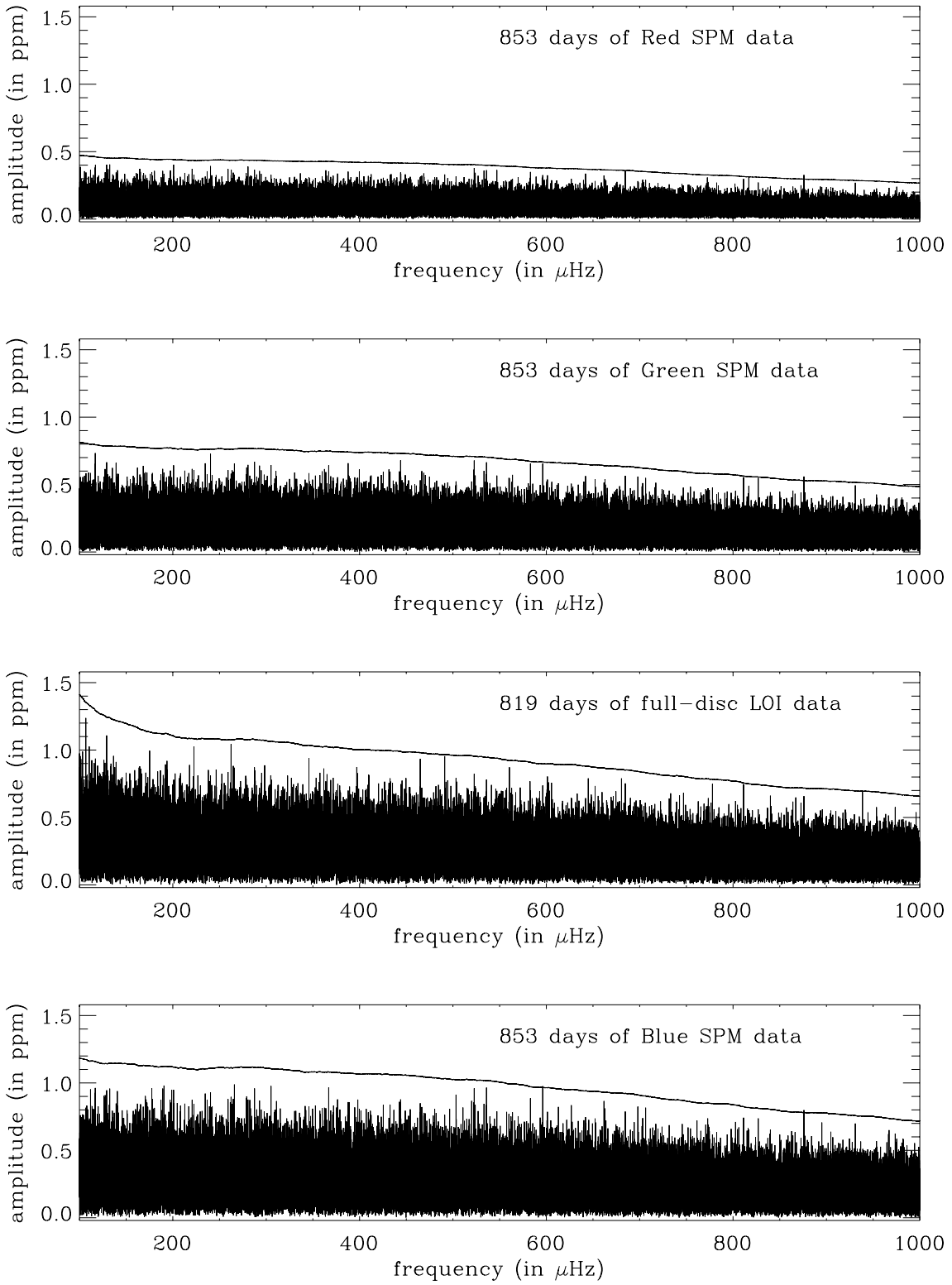
FIG. 1.— Full-disc intensity amplitude spectra for the three channels of the SPM and the full-disc LOI data. The continuous line gives the 0.1 probability limit that a peak be due to noise in a 70-μHz bandwidth. In the power spectrum, this level is about 10.8 $\tilde{s}$, i.e., about $\sqrt{10.8\tilde{s}}$ in the amplitude spectrum. Of course, $\tilde{s}$ differs for each of the spectra shown here.
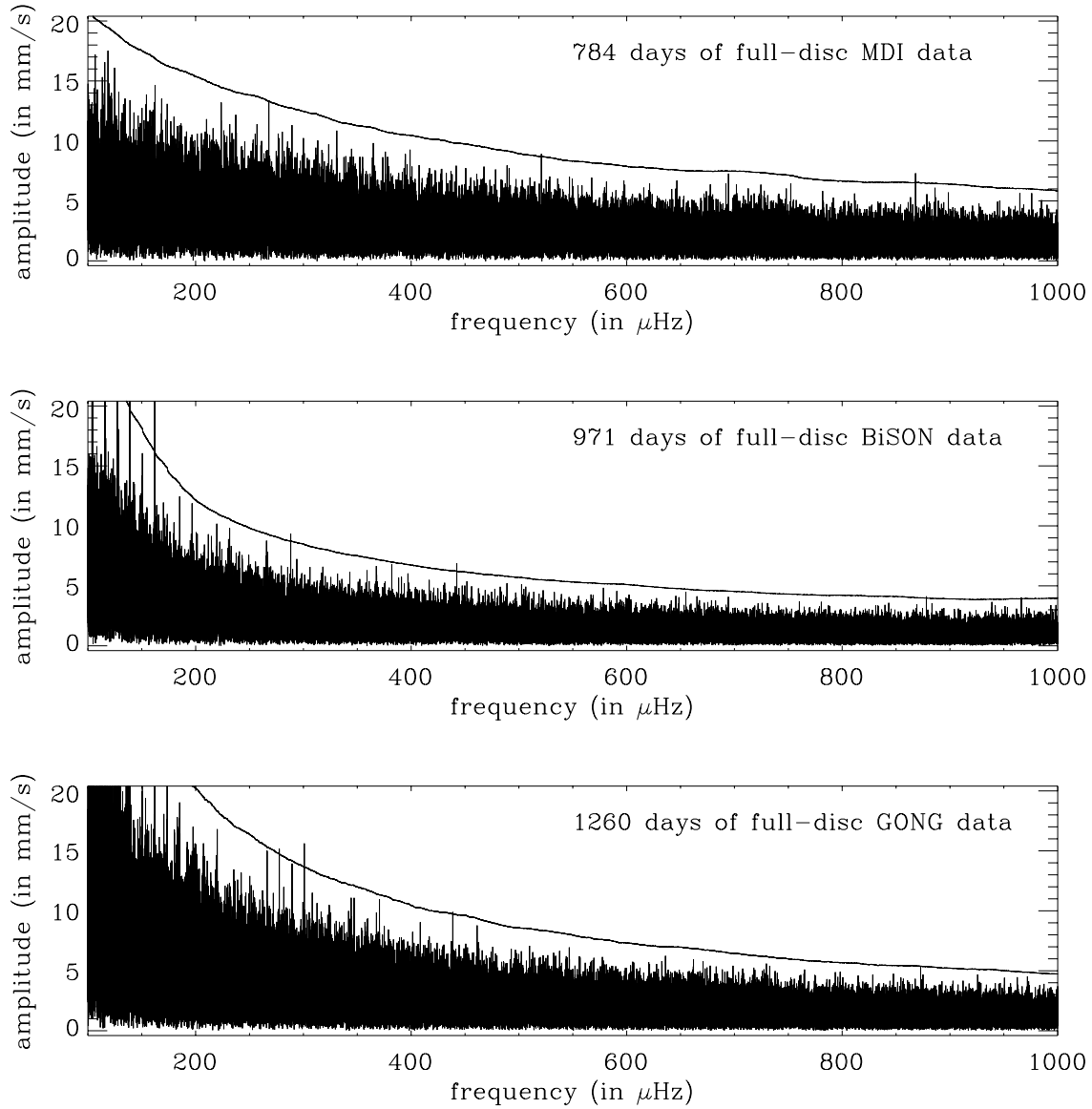
FIG. 2.— Full-disc velocity amplitude spectra for MDI (top), BiSON (middle) and GONG (bottom). The spectra are not corrected for the spatial filter functions. The continuous line gives the 0.1 probability limit that a peak be due to noise in a 70-μHz bandwidth. The limits in the amplitude spectra are $\sqrt{10.8\tilde{s}}$, $\sqrt{11.0\tilde{s}}$, $\sqrt{11.2\tilde{s}}$ for MDI, BiSON and GONG respectively. The MDI data contain harmonics of 52.125 μHz, which arise from beats between the spacecraft timing system and the instrument sampling rate. We have removed these from the spectrum displayed in the figure. Daily harmonics, which arise from data gaps in the time domain, are visible in the BiSON and GONG spectra at very low frequencies. Of course, $\tilde{s}$ differs for each of the spectra shown here.

where the splitting varies slowly; or (ii) over a whole range of possible splitting values. We have successfully applied this technique to detect low-frequency p modes in the GONG dataset (Appourchaux et al. 1998a; Rabello-Soares & Appourchaux 1999). Figure 3 illustrates how the $l = 2$, $n = 7$ mode is uncovered with the MDI data by the use of the collapsogramme. The shift of 399 nHz was optimally chosen as to reveal low-degree p modes.

As for standard power spectra, we can define a detection probability (p_{det}) which can be translated into a detection level s_{det} for the collapsogramme. The detection probability p_{det} is then related to s_{det} through the use of Eq. (8), where $x/2$ is now replaced by $(2l+1)s_{det}/\tilde{s}$. This yields:

$$p_{det} \approx T\Delta_{det}\left(\frac{\Gamma(2l+1,(2l+1)s_{det}/\tilde{s})}{\Gamma(2l+1)}\right) \qquad (14)$$

When $l = 0$, we recover an equation which can be solved analytically to yield Eq. (10). Note that we again chose $p_{det} = 0.1$ to maintain consistency with the previous section.

We have applied the collapsogramme technique to the LOI and MDI resolved data. We tried a range of splitting values from 200 to 1000 nHz, but were unable to find any peaks that were significantly above the background noise. Please note that when one looks at N collapsogrammes, the right-hand side of Eq. (14) should be multiplied by N. Therefore to keep the same probability level p_{det} when looking at N collapsogrammes, the detection level will increase accordingly.

Figs. 4 and 5 show typical collapsogrammes for $l = 1$ and 2. The 52.125-μHz beat has again been removed from the MDI spectra. As expected, the detection limits scale approximately as $1/\sqrt{2l+1}$.

In velocity, the best detection limit is obtained with MDI; at $l = 1$, it is about $11\,\mathrm{mm\,s^{-1}}$ at 200 μHz and $3.5\,\mathrm{mm\,s^{-1}}$ at 1000 μHz; for $l = 2$, it is about $9\,\mathrm{mm\,s^{-1}}$ at 200 μHz and $2.5\,\mathrm{mm\,s^{-1}}$ at 1000 μHz.

3.4. Analysis of combined data sets

Multivariate Spectral Regression Analysis (MSRA) can be used to determine the extent to which the variance in one time series is explainable in terms of the variance of other simultaneous series (Koopmans 1974). This is analogous to coincidence methods used in cosmic ray, nuclear and particle physics. A *multivariate process* produces vector-valued events, whose components may be dependent on each other up to a certain degree. Here, we consider the full-disc time series of solar irradiance in red, green, blue and total to be the 4 components of such a multivariate process. To enhance the signal of a resonant mode we look for similarities in the variance of these 4 components. If we assume that any mode present affects all the components in a similar manner, then one would expect its signature to appear rather-more prominently in the coherent part of the four channels.

For the simpler case of two channels, the coherent part would simply correspond to the channels multiplied by their cross coherence. However, where more than two channels are available we must use MSRA to determine the coherent part (Koopmans 1974). Unlike the two-channel case, MSRA is not symmetric in the sense that the coherence is calculated with respect to only one of the channels (termed the *independent* channel).

3.4.1. Multivariate Spectral Regression Analysis

MSRA explains the *dependent* component $Y(t)$ of a multivariate process by linearly filtering its n *independent* components $X(t)$, as

$$Y(t) = L(X(t)) + \eta(t), \qquad (15)$$

where $Y(t)$ is the 1-dimensional process of the dependent component and $X(t)$ are the n processes of the independent components. L is a multivariate linear filter with unknown n-dimensional transfer functions $B(\lambda)$ which transform the coherent part of the independent time series $X(t)$ into the coherent part of the dependent series $Y(t)$. $\eta(t)$ is the unobservable 1-dimensional residual (error) process that is not correlated with $X(t)$.

The extent to which $Y(t)$ deviates from a linear function of $X(t)$ is measured by the unknown *spectral density function* $f^{\eta}(\lambda) = \frac{dF^{\eta}(\lambda)}{d\lambda}$, where $F^{\eta}(\lambda)$ is the spectral distribution of $\eta(t)$. $f^{\eta}(\lambda)$ and the *transfer function* are the principal parameters of interest. $B(\lambda)$ indicates how the various inputs are parceled to the output series. They are determined by minimizing the expectation value $E[\eta^2(t)]$. The transfer function of B and the spectral density function of $\eta(t)$ can be calculated according to

$$B(\lambda) = f^{Y,X}(\lambda)f^{X}(\lambda)^{-1}, \qquad (16)$$

and

$$f^{\eta}(\lambda) = f^{Y}(\lambda) - f^{Y,X}(\lambda)f^{X}(\lambda)^{-1}f^{X,Y}(\lambda), \qquad (17)$$

where $f^{X}(\lambda)$, $f^{Y,X}(\lambda)$ and $f^{X,Y}$ are the power and cross spectral density functions of $X(t)$ and $Y(t)$; they are matrices of dimension $(n \times 1)$, $(n \times n)$, $(1 \times n)$, respectively (Koopmans 1974).

Moreover, one also recovers the *total coherence*, $\rho(\lambda)$, which is analogous to the correlation coefficient in linear regression analysis. The coherence squared corresponds to the fraction of $Y(t)$ explained by $L(X(t))$; so it is a direct measure of the signal-to-noise ratio. The total coherence is derived from

$$\rho^2(\lambda) = \frac{f^{Y,X}(\lambda)f^{X}(\lambda)^{-1}f^{X,Y}(\lambda)}{f^{Y}(\lambda)}, \qquad (18)$$

and the contribution of each process to the explained part is given by the complex n-dimensional partial coherence

$$\gamma(\lambda) = \frac{f^{X}(\lambda)^{-\frac{1}{2}}f^{Y,X}(\lambda)}{f^{Y}(\lambda)^{\frac{1}{2}}}. \qquad (19)$$
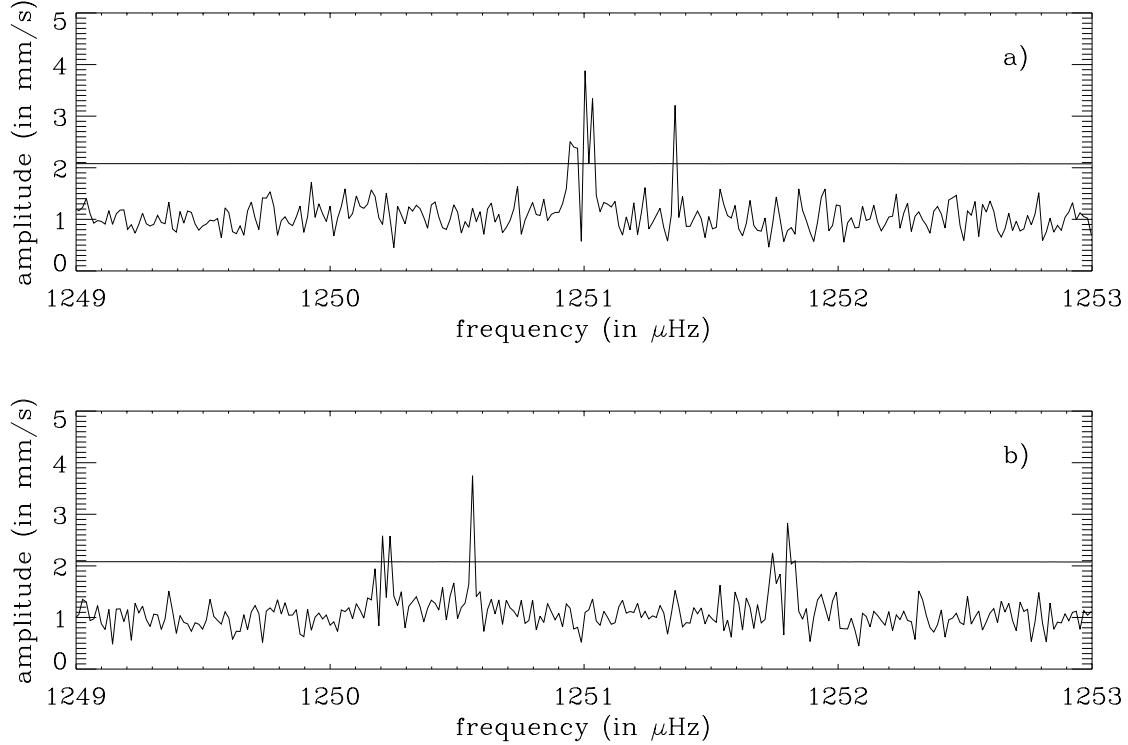
FIG. 3.— MDI collapsogramme for $l = 2$: unshifted (a), and shifted by Ω=399 nHz (b). The continuous line gives the 0.1 probability limit that a peak be due to noise in a 70 μHz bandwidth. In the amplitude spectrum, this level is about $\sqrt{4.0\bar{s}}$. This is to be compared with the value of $\sqrt{11.2\bar{s}}$ that would have been obtained from the full-disc amplitude spectrum. For the unshifted collapsogramme, the 0.1 probability limit was calculated assuming that the $2l + 1$ spectra are indeed uncorrelated. Since in reality this is not the case, the limit shown underestimates the true level. The dilution of the 52.125-μHz harmonics (at 1251 μHz in the upper panel) is quite effective; peaks at 1250.2 μHz and at 1251.8 μHz are the shifted harmonics for m=2 and m=-2, respectively. The $l = 2, n = 7$ stands out well at 1250.57 μHz in the lower panel. The main contribution comes from the $l = 2, m = +2$, already detected at 1251.4 μHz in the upper panel. Some contributions from the other m help improve the signal-to-noise ratio in the lower panel.
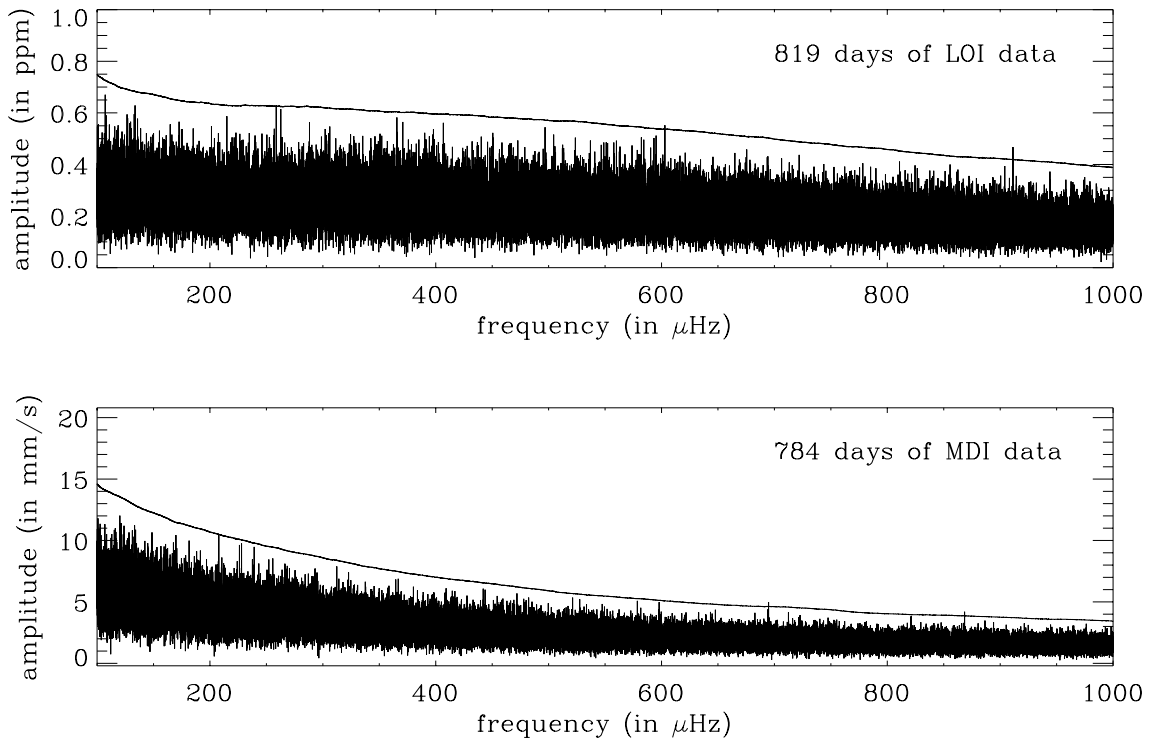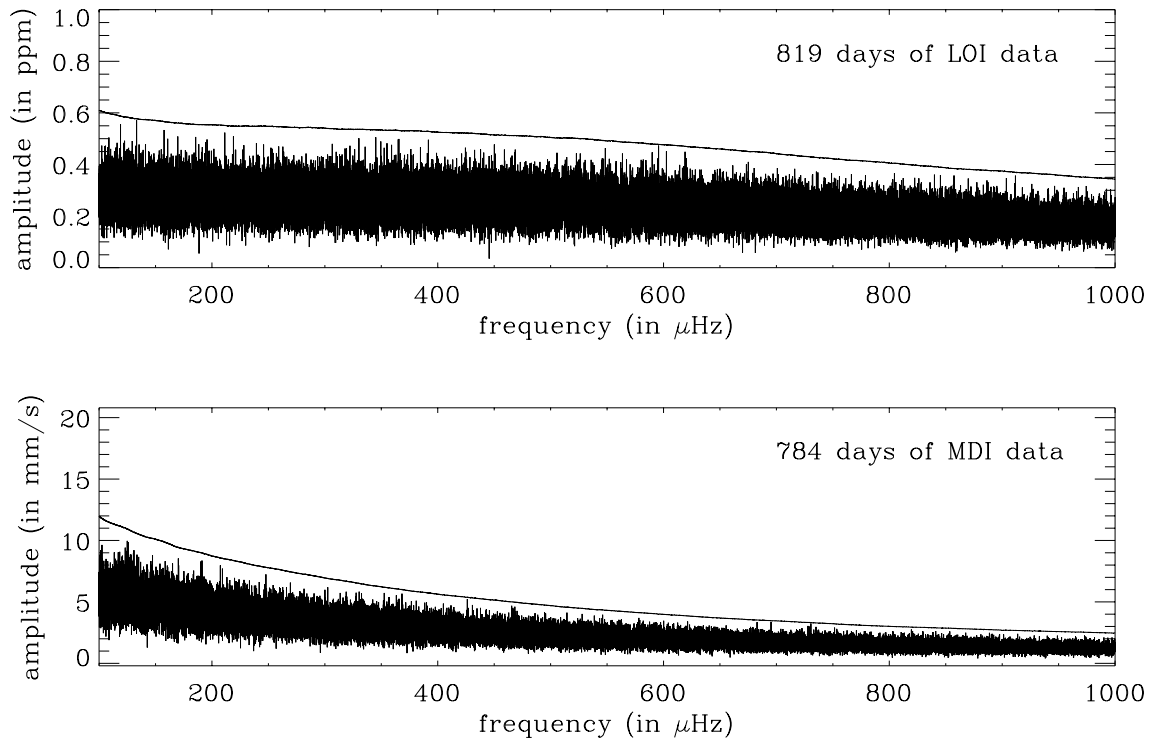
FIG. 4.— $l = 1$ collapsogramme for the LOI (top), MDI (bottom) resolved data, corrected for the spatial filter functions. The continuous line gives the 0.1 probability limit that a peak be due to noise in a 70 μHz bandwidth. The shift differs slightly between spectra since each was chosen to be an integer number of frequency bins (the observation times being different for each instrument). Note that while the magnitude of the shift is known to be valid for p modes, it is not expected to be so for g modes. The detection limit (in amplitude) is $\sqrt{5.3\bar{s}}$ both for LOI and MDI. This is to be compared with the $\sqrt{10.8\bar{s}}$ levels returned for the full-disc spectra.

FIG. 5.— $l = 2$ collapsogramme for the LOI (top), MDI (bottom) resolved data, corrected for the spatial filter functions. The continuous line gives the 0.1 probability limit that a peak be due to noise in a 70 μHz bandwidth. The shift differs slightly between spectra, since each was chosen to be an integer number of frequency bins (the observation times being different for each instrument). Note that while the magnitude of the shift is known to be valid for p modes, it is not expected to be so for g modes. The detection limits (in amplitude) is $\sqrt{3.9\bar{s}}$ both for LOI and MDI. This is to be compared with the $\sqrt{10.8\bar{s}}$ for the full-disc spectra.

$A^{-\frac{1}{2}}$ denotes the square root of the inverse of the matrix A and the sum of $|\gamma_i(\lambda)|^2$ equals $\rho^2(\lambda)$.

3.4.2. *Application to VIRGO full-disc data*

We applied MSRA to the TSI time series measured by the PMO6 radiometer and the three spectral channels of the SPM, i.e., we selected TSI to be the independent channel and then calculated simultaneously the coherent part of all three colored channels with respect to the TSI. We set $Y(t)$ to the TSI time series and $X(t)$ to the three spectral time series and calculated the corresponding spectral density functions $f^{\mathrm{PMO6}}(\lambda)$ and $f^j(\lambda)$ (j = red, green, blue). From the *smoothed* density functions we calculated the transfer functions $B_j(\lambda)$, according to Eq. (16). Smoothing is necessary since the individual frequency bins of the density functions would otherwise be independent of each other, with the result that the coherence would then always be unity. The range of smoothing must be sufficiently large to achieve a certain confidence level, but also small enough to allow the power of a possible g mode to be of a similar level as the remaining noise power. We applied a boxcar running mean of 35 bins $\simeq 0.46\ \mu$Hz width. The total coherence squared in the g-mode range is about 0.8. This means that 80% of the variance of TSI (power in the spectrum) can be explained by the time series of the red, green and blue channels. Since the four instruments are on the same platform, the coherence is due not only to common solar noise, but also to common instrumental noise. Nevertheless, we believe that the main contribution is the Sun itself.

From the $f^j(\lambda)$ original, unsmoothed, Fourier spectra of the red, green, and blue channels of the SPM, we can calculate the coherent part of the 3 spectra with respect to the TSI spectrum according to:

$$f^{\mathrm{coh}}(\lambda) = \sum_{j=r,g,b} B_j(\lambda) f^j(\lambda). \qquad (20)$$

Here $f^{\mathrm{coh}}(\lambda)$ is the sum of all coherent features in the SPM spectra with respect to the PMO6 spectrum. If the signature of some resonant mode appears in any of the SPM spectra, it will also appear in the TSI spectrum, since these measurements also contain the response at the three colored wavelengths (but not *vice versa*). Therefore, provided the signature is present in at least one of the SPM spectra, we can be sure that it will also appear in the coherent part. This argument does not hold if the signature of some resonant mode appeared only in the TSI. This could be the case if, for example, the mode signature were much stronger at infrared wavelengths (i.e., $> 1\mu$m), that are not sampled by the SPM. In this case the infrared signal would be seen in the *incoherent residual* of the MSRA.

$$f^{\mathrm{incoh}}(\lambda) = f^{\mathrm{PMO6}}(\lambda) - f^{\mathrm{coh}}(\lambda) = f^{\mathrm{PMO6}}(\lambda) - \sum_{j=r,g,b} B_j(\lambda) f^j(\lambda),$$
$$(21)$$

with $f^{\mathrm{PMO6}}(\lambda)$ the original, unsmoothed, Fourier spectrum of the TSI.

The method of analyzing the coherent part (Eq. 20) has been tested by introducing artificial modes into the VIRGO data. We added 100 sine waves of constant amplitude to the time series of all three SPM channels, and that of the TSI. In the coherent part $f^{\mathrm{coh}}(\lambda)$ of the spectra, the amplitude ratio of these sine waves was amplified by up to a factor of 2 with respect to the ambient noise level. While this certainly constitutes an improvement, it is nevertheless insufficient to reveal any g modes.

Figure 6 shows the results of the MSRA analysis for the SPM and PMO6 data. The residual spectrum does not show any evidence for g modes or very low-frequency p modes. The peaks that are visible arise from beats between the VIRGO and spacecraft timing. As noted earlier, a similar phenomenon is present in the MDI data.

3.4.3. *Application to velocity-intensity data*

A similar MSRA analysis was performed between the PMO6 intensity and MDI velocity data (Fig. 7). Here the coherence between the instruments is rather low, which implies that the solar noise in both intensity and velocity is largely uncorrelated. This fact is yet to be fully utilized in attempts to extract undetected low-frequency p modes.

4. DISCUSSION

The theoretical predictions of the expected amplitudes of solar internal g modes are at best very uncertain. Uncertainty arises from our inability to describe adequately the nature of the interaction of the modes with the convection zone and the solar atmosphere. The possibility that low-order g modes are overstable is probably no longer of relevance: amplitude limitation by three-mode resonant coupling to a stable pair of g modes of higher degrees seems likely to prevent overstable modes from achieving observable amplitudes (Dziembowski 1983, Jordinson & Gough 2000)

Andersen (1996) and Kumar et al. (1996) have recently reconsidered the problem of the excitation of g modes by turbulence in the convection zone, in somewhat different manners. Both derive similar estimates of upper limits. The larger spread in possible mode amplitudes presented by Andersen (1996) may be due to an inadequate treatment of mode damping. The upper limits for low-order g modes derived in these studies are in the range 0.01 to $1\ \mathrm{mm\,s^{-1}}$.

The transformation of a theoretical g-mode $\delta R/R_\odot$ perturbation to an observable Doppler shift or intensity variation is a non-trivial problem. Several papers have addressed the issues involved (Dziembowski 1977, Berthomieu & Provost 1990 and Toutain & Gouttebroze 1993, Toutain et al. 1999). Further, the determination of the theoretical conversion factor between velocity and intensity perturbations is fraught with difficulties. The simplistic approach of Isaak (1980) is to adopt
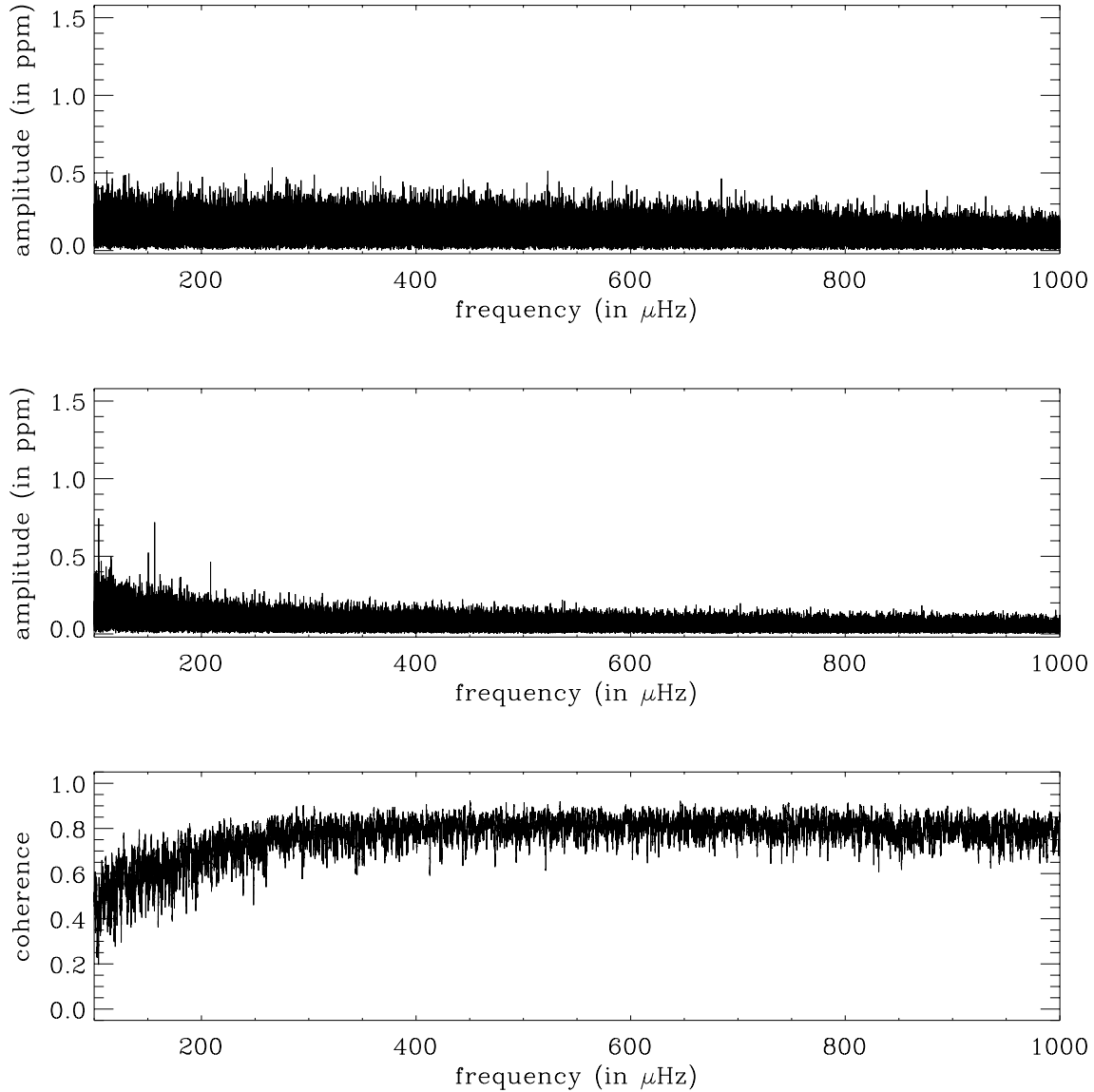
FIG. 6.— MSRA analysis of the SPM and PMO6 data: coherent part (top), incoherent part (middle), and coherence (bottom). Three out of four of the most prominent peaks are harmonics of 52.125 μHz that arise from beats between the VIRGO instrument and spacecraft timing. This phenomenon is also observed in the MDI data.
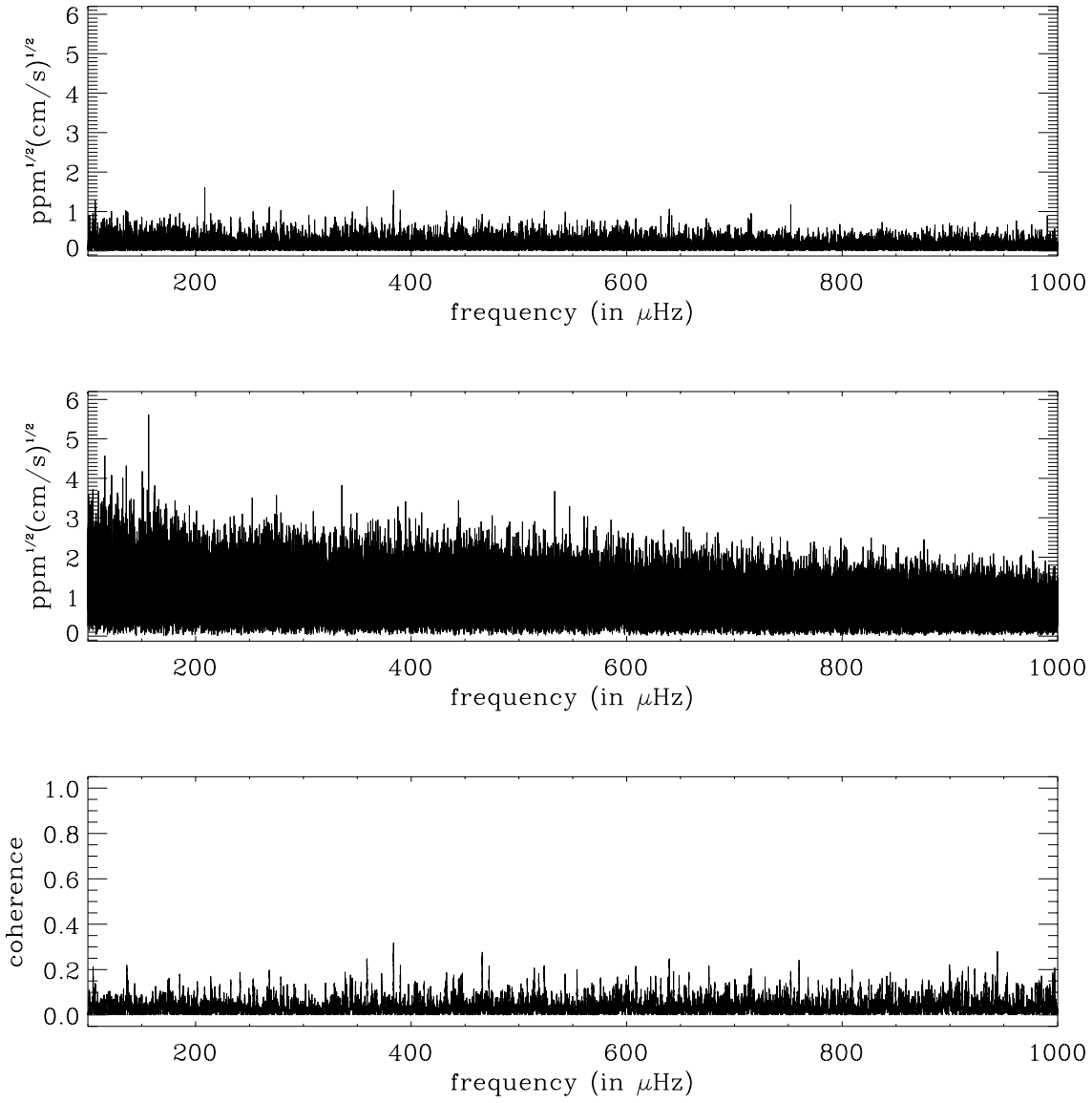
FIG. 7.— MSRA analysis of 784 days of coeval MDI velocity and PMO6 intensity data: coherent part (top), incoherent part (middle), and coherence (bottom).

the value appropriate to Cepheid variable, namely about $4\ \mathrm{cm\,s^{-1}\,ppm^{-1}}$. Theoretical calculations (Toutain et al. 1996, Houdek 1996) indicate that the ratio is strongly dependent on the frequency of oscillation, and give values for $l = 1$ of 50 to $80\,\mathrm{cm\,s^{-1}\,ppm^{-1}}$ for oscillations with frequency near 200 μHz. For higher value of l the results give numbers in the range 1 to 10 $\mathrm{cms^{-1}ppm^{-1}}$. However, both of these calculations are deficient in potentially serious respects: Houdek's calculations (which have been extended to $\nu = 200\mu\mathrm{Hz}$, yielding the ratio $80\,\mathrm{cm\,s^{-1}\,ppm^{-1}}$) are strictly applicable to radial modes, and therefore account for neither the non-radial geometrical complexities of the radiative transfer in the atmosphere nor the effect of shear on the convective heat and momentum fluxes, whereas in the non-radial calculations of Toutain et al. convective flux perturbations are ignored altogether. If we adopt cautiously the above values, they indicate that for velocity amplitudes of a few millimeters per second we might expect intensity perturbations for low-degree g modes of below 0.01 ppm. These theoretical upper-limit estimates are well below the observational limits set by the work presented here. Here we must also point that by comparing the MDI and GOLF data (Henney et al. 1999), we can derive, as defined above in this paper, a 10% detection limit for GOLF of about $10\,\mathrm{mm\,s^{-1}}$. This is similar to the limit given in this paper. The limits set by our data suggest that the g-mode candidates of Gabriel et al. (1998) are more likely to be due to the solar noise because we are unable to detect and identify any significant peaks with an amplitude of $8\,\mathrm{mm\,s^{-1}}$ in the range 200 to 300 μHz, even if the modes are present.

In addition, we should make the reader aware that such lack of detection is consistent with the prediction by Gough (1985) and Harvey (1985). Gough predicted g-mode amplitudes no greater than $1\,\mathrm{mm\,s^{-1}}$ using turbulent stochastic excitation, while Harvey predicted a $1-\sigma$ solar noise of about 8 $\mathrm{mms^{-1}}$ for a 2-year time series. Clearly solar noise at such a level would have prevented us from detecting the g modes, even if this noise was found to be lower by about a factor 2 (Elsworth et al. 1994, Henney et al. 1999).

Given our current prejudices regarding the expected characteristics of core-penetrating g modes, it therefore seems unlikely that a firm, unambiguous detection will be made in the near future by one instrument or network alone using straightforward Fourier techniques. For example, an improvement in the signal-to-noise ratio in amplitude from single-instrument data by a factor ten – assuming a stable noise power spectral density, and a coherent mode signature over the duration of the observations – requires a factor hundred-fold increase in observing time. A coordinated, coherent approach that involves the utilization of contemporaneous data from the various active observational programs would seem to offer the best prospect of future progress. Further improvements may also come from concentrating our attentions at the solar limb. There is observational evidence to suggest that the p-mode intensity signal is amplified at the limb with respect to the disc-center values (Appourchaux & Toutain 1998, Toner et al. 1999), an effect that the PICARD instrument will attempt to take advantage of (Damé et al. 1998) in its efforts to detect g modes.

5. CONCLUSION

Nearly contemporaneous, high-quality data from both space (MDI, VIRGO on board SOHO) and ground-based (BiSON, GONG) observations have been used in an attempt to detect solar g modes. We have applied statistical analyses, a Multivariate Spectral Analysis (MSRA), and pattern-recognition techniques to these data. Although we have been unable to uncover the presence of a g-mode signature, we have nevertheless established firm upper-limit estimates to their amplitudes. These are defined as the level at which a peak has only a 10-% probability of appearing by chance over a 70-μHz bandwidth. At a frequency of $\sim 200\,\mu$Hz the statistical approach yields an upper limit of about 10 $\mathrm{mms^{-1}}$ in velocity, and 0.5 ppm in intensity. The MSRA gives a slightly lower limit. The results confirmed theoretical prediction regarding the non-detectability of the solar g modes.

APPENDIX

SPATIAL FILTER FUNCTION CALCULATION

Definition of the spatial filter function

Let us suppose that $q(\theta, \phi, t)$ is some physical quantity (say, velocity) on the Sun expressed as:

$$q(\theta, \phi, t) = \sum_{l,m} q_{l,m}(t) Z_l^m(\theta, \phi) \tag{A1}$$

where t is the time, (θ, ϕ) are the spherical coordinates, $q_{l,m}(t)$ represents the time dependence of the oscillation generated by stochastic oscillations and $Z_l^m(\theta, \phi)$ describes the horizontal variation of the radial velocity (or intensity) whose normalization is defined as:

$$\frac{1}{4\pi} \int_\Omega |Z_l^m(\theta, \phi)|^2 d\Omega' = 1 \tag{A2}$$

where Ω represents the solar sphere. Observation and data analysis procedures produce the observed component $Q(t)$. The observable $Q(t)$ is derived from the local perturbation. For instance, the line-of-sight velocity is derived from the horizontal and vertical displacements, while the intensity is derived from opacity and temperature perturbations. The observable $Q_{l',m'}(t)$ is assumed to have the form:

$$Q_{l',m'}(t) = \int_{\mathcal{D}_\odot} q(\theta, \phi, t) D_{l'}^{m'}(\theta, \phi) d\Omega \tag{A3}$$

where $\mathcal{D}_\odot$ is the visible solar disc and $D_m^l(\theta, \phi)$ is a weight applied to the solar disc for extracting the (l, m) mode signal. $D_m^l(\theta, \phi)$ depends on the way the observation has been made and also on the data analysis procedure; it includes the projection effect, limb darkening (if applicable), and the (l, m) mask and any other factor that might arise from the procedure. Putting Eq. A1 into Eq. A3, we get:

$$Q_{l',m'}(t) = \sum_{l,m} q_{l,m}(t) \int_{\mathcal{D}_\odot} Z_l^m(\theta, \phi) D_{l'}^{m'}(\theta, \phi) d\Omega \tag{A4}$$

$$= \sum_{l,m} q_{l,m}(t) s_{l,m}^{l',m'} \tag{A5}$$

where

$$s_{l,m}^{l',m'} = \int_{\mathcal{D}_\odot} Z_l^m(\theta, \phi) D_{l'}^{m'}(\theta, \phi) d\Omega \tag{A6}$$

When there is only one component 'present', i.e. $l = l'$ and $m = m'$, then $Q(t) = S_{l,m} q_{l,m}(t)$, and the RMS amplitude of the observed signal is related to the RMS amplitude of the perturbation via:

$$< Q(t) > = |S_{l,m}| < q_{l,m}(t) > \tag{A7}$$

where $S_{l,m}$ is defined as:

$$S_{l,m} = \int_{\mathcal{D}_\odot} Z_l^m(\theta, \phi) D_l^m(\theta, \phi) d\Omega \tag{A8}$$

Spatial filter function for velocity

Perturbation

The velocity is the derivative of the displacement. We have assumed that the main contribution to the velocity is a vertical displacement whose spatial distribution is proportional to the spherical harmonics. Therefore, we have for the vertical velocity:

$$Z_l^m(\theta, \phi) = \sqrt{4\pi} Y_l^m(\theta, \phi) \tag{A9}$$

where $Y_l^m(\theta, \phi)$ are the spherical harmonics.

Full-disc calculation

For full-disc velocity observation, the weight function is given by:

$$D_l^m(\theta, \phi) = \frac{I(\sin\theta\cos\phi)\sin^2\theta\cos^2\phi}{\int_{\mathcal{D}_\odot} I(\sin\theta\cos\phi)\sin^2\theta\cos\phi d\theta d\phi}, \tag{A10}$$

where I is the intensity on the solar disk. Thus the spatial filter function can be written as:

$$S_{l,m}^{\text{BiSON}} = \frac{\sqrt{4\pi}\int_{\mathcal{D}_\odot} Y_l^m(\theta,\phi)I(\sin\theta\cos\phi)\sin^3\theta\cos^2\phi d\theta d\phi}{\int_{\mathcal{D}_\odot} I(\sin\theta\cos\phi)\sin^2\theta\cos\phi d\theta d\phi}. \tag{A11}$$

Imaging instrument calculation

For resolved velocity observations, the weight function is given by:

$$D_l^m(\theta, \phi) = \frac{1}{n_{l,m}}Y_l^{m*}(\theta,\phi)\sin^2\theta\cos^2\phi \tag{A12}$$

where the symbol * denotes the complex conjugate and $n_{l,m}$ is a normalization factor. Depending on how the data reduction is performed, the normalization may vary. In the case of MDI, $n_{l,m}$ is chosen such that:

$$S_{l,m}^{\text{MDI}} = 1 \tag{A13}$$

Spatial filter function for intensity

Perturbation

For intensity, the main contribution was assumed to come from the perturbation of the temperature. This is an approximation because opacity perturbations and surface distortions should also be included. In this case we also have:

$$Z_l^m(\theta, \phi) = \sqrt{4\pi}Y_l^m(\theta, \phi) \tag{A14}$$

Full-disc calculation

For full-disc intensity observations, the weight function is given by:

$$D_l^m(\theta, \phi) = \frac{I(\sin\theta\cos\phi)\sin\theta\cos\phi}{\int_{\mathcal{D}_\odot} I(\sin\theta\cos\phi)\sin^2\theta\cos\phi d\theta d\phi} \tag{A15}$$

and the spatial filter function can be written as:

$$S_{l,m}^{\text{SPM}} = \frac{\sqrt{4\pi}\int_{\mathcal{D}_\odot} Y_l^m(\theta,\phi)I(\sin\theta\cos\phi)\sin^2\theta\cos\phi d\theta d\phi}{\int_{\mathcal{D}_\odot} I(\sin\theta\cos\phi)\sin^2\theta\cos\phi d\theta d\phi} \tag{A16}$$

Imaging instrument calculation

The LOI is an imaging intensity instrument with pixels that are rather large compared to the degrees to be observed. A continuous calculation is not proper. The spatial filter function is then derived from the way the pixel data is combined:

$$S_{l,m} = \frac{1}{3}\sum_i w_i^{(l,m)*}\tilde{y}_i^{(l,m)} \tag{A17}$$

where $\tilde{y}_i^{(l,m)}$ is the spatial filter function of pixel i given by:

$$\tilde{y}_i^{(l,m)} = \frac{\sqrt{4\pi}\int_{\mathcal{D}_i} Y_l^m(\theta,\phi)I(\sin\theta\cos\phi)\sin^2\theta\cos\phi d\theta d\phi}{\int_{\mathcal{D}_i} I(\sin\theta\cos\phi)\sin^2\theta\cos\phi d\theta d\phi} \tag{A18}$$

where $\mathcal{D}_i$ is the integration domain of the i-th LOI pixel. The weights applied are then:

$$w_i^{(l,m)} = \frac{\tilde{y}_i^{(l,m)}}{\sqrt{\sum_i \tilde{y}_i^{(l,m)*} \tilde{y}_i^{(l,m)}}} \qquad (A19)$$

and the spatial filter function is written as:

$$S_{l,m}^{\mathrm{LOI}} = \sqrt{\frac{1}{9} \sum_i \tilde{y}_i^{(l,m)*} \tilde{y}_i^{(l,m)}} \qquad (A20)$$

<div align="center">REFERENCES</div>

Andersen B. N. 1996, A&A, 312, 610

Anklin M., Fröhlich C., Finsterle W., Crommelynck D. A., Dewitte S. 1998, Metrologia, 35, 686

Appourchaux T., Andersen B., Chaplin W., Elsworth Y., Finsterle W., Fröhlich C., Gough D., Hoeksema J. T., Isaak G., Kosovichev A., Provost J., Scherrer P., Sekii T., Toutain T. 1998a, in S. Korzenik, A. Wilson (eds.), Structure and Dynamics of the Interior of the Sun and Sun-like Stars, ESA SP-418, ESA Publications Division, Noordwijk, The Netherlands, p. 95

Appourchaux T., Andersen B., Fröhlich C., Jimenez A., Telljohann U., Wehrli C. 1997, Sol. Phys., 170, 27

Appourchaux T., Andersen B. N. 1990, Sol. Phys., 128, 91

Appourchaux T., Gizon L., Rabello-Soares M. C. 1998b, A&AS, 132, 107

Appourchaux T., Toutain T. 1998, in J. Provost, F.-X. Schmider (eds.), Sounding solar and stellar interiors – IAU 181 – Poster volume, 5

Berthomieu G., Provost J. 1990, A&A, 227, 563

Brookes J. R., Isaak G. R., van der Raay H. B. 1976, Nature, 259, 92

Brookes J. R., Isaak G. R., van der Raay H. B. 1978a, MNRAS, 185, 19

Brookes J. R., Isaak G. R., van Der Raay H. B. 1978b, MNRAS, 185, 1

Brown T. M., Stebbins R. T., Hill H. A. 1978, ApJ, 223, 324

Christensen-Dalsgaard J. 1989, MNRAS, 239, 977

Christensen-Dalsgaard J. 1998, in S. Korzenik, A. Wilson (eds.), Structure and Dynamics of the Interior of the Sun and Sun-like Stars, ESA SP-418, ESA Publications Division, Noordwijk, The Netherlands, 17

Damé L., Hersé M., Thuillier G., Appourchaux T., Crommelynck D., Dewitte S., Joukoff, A. Fröhlich C., Laclare F., Delmas C., Boumier P. 1998, Adv. Space Research, 24 (2), 295

Delache P., Scherrer P. H. 1983, Nature, 306, 651

Denison D. G. T., Walden A. T. 1999, ApJ, 514, 972

Dziembowski W. 1977, Acta Astronomica, 27, 203

Dziembowski W. A. 1983, Sol. Phys., 82, 259

Elsworth Y., Howe R., Isaak G. R., McLeod C. P., Miller B. A., New R., Speake C. C., Wheeler S. J. 1994, MNRAS, 269, 529

Elsworth Y., Howe R., Isaak G. R., McLeod C. P., Miller B. A., van Der Raay H. B., Wheeler S. J., New R. 1995, in ASP Conf. Ser. 42: GONG 1992. Seismic Investigation of the Sun and Stars, p. 392

Fröhlich C., Andersen B. N. 1995, in J. T. Hoeksema, V. Domingo, B. Fleck, B. Patrick (eds.), Forth SOHO Workshop: Helioseismology (Invited Reviews), ESA-SP-376, Noordwijk NL, p. 137

Fröhlich C., Delache P. 1984, in R. K. Ulrich, J. Harvey, E. J. Rhodes, J. Toomre (eds.), Solar Seismology from Space, JPL Publ.84-84, Pasadena, p. 183

Fröhlich C., Romero J., Roth H., Wehrli C., Andersen B. N., Appourchaux T., Domingo V., Telljohann U., Berthomieu G., Delache P., Provost J., Toutain T., Crommelynck D. A., Chevalier A., Fichot A., Dappen W., Gough D., Hoeksema T., Jimenez A., Gomez M. F., Herreros J. M., Cortès T. R., Jones A. R., Pap J. M., Willson R. C. 1995, Sol. Phys., 162, 101

Gabriel A., Turck-Chièze S., García R., Pallé P., Boumier P., Thiery S., Grec G., Ulrich R., Bertello L., Roca Cortés, Robillot J.-M. 1998, in S. Korzenik, A. Wilson (eds.), Structure and Dynamics of the Interior of the Sun and Sun-like Stars, ESA SP-418, ESA Publications Division, Noordwijk, The Netherlands, 61

Gough D. O. 1985, in E. Rolfe, B.Battrick (eds.), Future Missions in Solar, Heliospheric and Space Plasma Physics, ESA SP-235, ESA Publications Division, Noordwijk, The Netherlands, p. 183

Harvey J. 1985, in E. Rolfe, B.Battrick (eds.), Future Missions in Solar, Heliospheric and Space Plasma Physics, ESA SP-235, ESA Publications Division, Noordwijk, The Netherlands, p. 199

Harvey J., Hill F., Hubbard R., Kennedy J., Leibacher J., Pintar J., Gilman P., Noyes R., Title A., Toomre J., Ulrich R., Bhatnagar A., Kennewell J., Marquette W., Patrón J., Saá O., Yasukawa E. 1996, Science, 272, 1284

Henney C. J., Ulrich R. K., Bertello L., Bogart R. S., Bush R. I., Scherrer P. H., Cort/'es T. R., Turck-Chièze S. 1999, A&A, 348, 627

Hill F., Stark P., Stebbins R., Anderson E., Antia H., Brown T., Duvall, Jr. T., Haber D., Harvey J., Hathaway D., Howe R., Hubbard R., Jones H., Kennedy J., Korzennik S., Kosovichev A., Leibacher J., Libbrecht K., Pintar J., Rhodes, Jr. E., Schou, J. Thompson M., Tomczyk S., Toner C., Toussaint R., Williams W. 1996, Science, 272, 1292

Hoeksema J., Bush R., Mathur D., Morrison M., Scherrer P. 1998, IAU Symposia, 181, 31

Hoogeveen G. W., Riley P. 1998, Sol. Phys., 179, 167

Houdek G. 1996, *Ph.D. thesis*, Universität Wien

Isaak G. R. 1980, Nature, 283, 644

Jones H. P. 1989, Sol. Phys., 120, 211

Jordinson C., Gough D. 2000, in L.Szabados, D.W.Kurtz (eds.), The impact of large-scale surveys on pulsating-star research, in press

Koopmans L. 1974, The Spectral Analysis of Time Series, Academic Press, Inc., London, GB

Kumar P., Quataert E. J., Bahcall J. N. 1996, ApJ, 458, L83

Marsden R. G., Smith E. J., Cooper J. F., Tranquille C. 1996, A&A, 316, 279

Rabello-Soares M. C., Appourchaux T. 1999, A&A, 345, 1027

Riley P., Sonett C. P. 1996, Geophys. Res. Lett., 23, 1541

Scherrer P. H., Bogart R. S., Bush R. I., Hoeksema J. T., Kosovichev A. G., Schou J., Rosenberg W., Springer L., Tarbell T. D., Title A., Wolfson C. J., Zayer I., Mdi Engineering Team 1995, Sol. Phys., 162, 129

Scherrer P. H., Wilcox J. M., Kotov V. A., Severny A. B., Tsap T. T. 1979, Nature, 277, 635

Severny A. B., Kotov V. A., Tsap T. T. 1976, Nature, 259, 87

Thomson D. J., Maclennan C. G., Lanzerotti L. J. 1995, Nature, 376, 139

Toner C. G., Jefferies S. M., Toutain T. 1999, ApJ, 518, L127

Toutain T., Berthomieu G., Provost J. 1999, A&A, 344, 188

Toutain T., Berthomieu G., Provost J., Gouttebroze P. 1996, in J. Hoeksema, V. Domingo, B. Fleck, B. Battrick (eds.), 4th SOHO workshop – Helioseismology – Vol 2, ESA SP-376, ESA Publications Division, Noordwijk, The Netherlands, p. 419

Toutain T., Gouttebroze P. 1993, A&A, 268, 309